Journal Pre-proof

Machine learning aided modelling of thermomechanical fatigue of solder joints in electronic component assemblies

Vincent Voet, Frederik Van Loock, Christophe De Fruytier, Aude Simar, Thomas Pardoen

PII: S0142-1123(22)00548-5
DOI: https://doi.org/10.1016/j.ijfatigue.2022.107298
Reference: JIJF 107298

To appear in: *International Journal of Fatigue*

Received date : 10 June 2022
Revised date : 22 September 2022
Accepted date : 22 September 2022

Machine learning aided modelling of thermomechanical fatigue of solder joints in electronic component assemblies

Vincent Voet[a,b], Frederik Van Loock[a], Christophe De Fruytier[b], Aude Simar[a], Thomas Pardoen[a]

[a] *Institute of Mechanics, Materials and Civil Engineering, IMAP, UCLouvain, 1348 Louvain-la-Neuve, Belgium*
[b] *Thales Alenia Space Belgium, 6032 Mont-sur-Marchienne, Belgium*

Abstract

Printed board assemblies, i.e. components soldered on printed circuit boards (PCBs), are exposed to thermal cycles responsible for fatigue cracking of solder joints as a result of thermal expansion mismatch between the constituting elements. Advanced finite element simulations are performed using a traction-separation law to represent the cracking process and a temperature-dependent elasto-viscoplastic model for the joint response. Predictions are successfully assessed towards machine learning processed experimental data. In particular, the high sensitivity of thermal ageing reliability to geometric dimensions and solder joint thickness is properly captured. Additional parameters, related to the PCB substrate, are also studied, opening new avenues towards design optimization.

Keywords:
solder joints, cohesive zone modeling, machine learning, thermomechanical fatigue

1. Introduction

Electronic assemblies for space applications have to meet very high standards in terms of quality and reliability. These assemblies comprise multiple electronic components soldered on printed circuit boards (PCBs). During operation, they are exposed to thermal cycling due to e.g. the satellite's orbit and/or interrupted operating modes. Mismatches in the coefficients of thermal expansion of the assembly's materials, i.e. those of the electronic components, tin-lead solder joints [1] and PCBs, lead to cyclic deformation and fatigue damage accumulation within the solder layer [1, 2, 3, 4]. The toughness and fatigue crack growth resistance of the soldered joint, and, therefore, the reliability of the assembly, is dominated by the elasto-viscoplastic deformation response and the damage resistance of the tin-lead solder material [5, 6]. The level of reliability is also affected by the manufacturing conditions. Several soldering processes can be used such as reflow and iron soldering, leading to different thermomechanical histories, void distributions and solder joint thicknesses. The variability associated with the mounting process is significantly large, even more with manual soldering.

The reliability of solder joints has been studied for more than half a century in a wide range of industrial fields [7, 8, 9]. Several experimental methods have been developed to characterize the behaviour of electronic assemblies under cyclic thermal loadings. These include (i) micro-sectioning, where electronic assemblies are trimmed, moulded in epoxy resin and, finally, polished to be observed with a microscope and (ii) electrical monitoring, where continuous resistance measurements are conducted. Failure is detected by an increase in the recorded resistance due to the presence of a crack. Both methods are approved by the European Space Agency (via the ECSS standards), and are commonly used in the space industry.

Modelling approaches have also been developed to determine the reliability of electronic assemblies when subjected to thermal cycles and to justify accelerated cyclic tests by converting temperature profiles from test to operating (actual) conditions. Analytical models, such as the laws of Norris-Landzberg [10] and Engelmaier [11], have been developed to predict the re-

[1] Lead-based alloys are still used in the space industry due to the requirement of material joining methods with proven assembly reliability.

liability of a solder joint (in terms of thermal cycles to failure) for a given cyclic temperature profile, characterized by the mean temperature, temperature range, and cycle frequency. Analytical approaches are commonly used in industry, but suffer from a limited window of validity: they make use of empirical parameters with limited validity in terms of temperature range and frequency. In addition, multiple damage mechanisms may co-exist in the solder joint and govern solder failure, which proves to be challenging to capture via analytical laws [12]. Numerical models using finite element analysis with various damage criteria, based on the inelastic or total strain or inelastic work, have been proposed in the literature [3, 13]. The formulation and identification of these models require an improved understanding of the thermomechanical and fatigue behaviour of the assembly. These more advanced methods are expected to overcome some of the limitations encountered by analytical approaches such as an extended working range. Damage mechanics approaches have been developed to get rid of the geometry dependence of fatigue laws [12]. These include cohesive zones models, which allow explicit simulations of crack propagation [14], and continuum damage methods [15, 16], where damage-dependent parameters are used to dictate the constitutive behaviour of the joint material. These models offer an in-depth understanding of solder joint damage but are not taking advantage of a machine learning approach to process experimental data that allows improving the reliability of parametric studies.

Advanced numerical models rely on many material parameters and many underlying assumptions regarding the description of the failure process; hence, they have to be validated for a wide range of electronic assembly configurations. However, testing all conditions is cumbersome and very challenging from a practical point of view. This motivates the use of a machine learning algorithm to process available experimental data and isolate individual parameters of interest and hence, provide extended model parameter identification and validation capabilities. It allows a better and more reliable determination of how characteristic parameters influence joint failure.

The objective of the present study is to develop and validate an innovative approach based on experimental data collected by the company Thales Alenia Space for decades and processed through a neural network. The available data involves many variations of parameters and can hardly be used without treatment for model comparison assessments. Thermally aged assembly data mainly consists of micro-sections observed by microscopy. Data extracted from these samples are compiled and used to train and test the fully connected neural network model. The latter allows the identification of parameters and the validation of an advanced finite element model. A traction-separation law is used to simulate the fatigue crack advance. Cohesive zone elements are located at the interface between the component and the joint, in the region where cracks are prone to propagate in ceramic surface-mounted resistors. The material behaviour of the solder joint is elastic-viscoplastic with temperature dependence. Compared to most literature studies, crack initiation and propagation is captured for a large number of applied thermal cycles. Various assembly configurations are tested in the scope of the parametric study. The ultimate goal is to identify design guidelines and to estimate assembly reliability based on such an advanced thermomechanical model.

The paper is structured as follows: section 2 presents the experimental analysis, including the description of the solder joint test method and the machine learning algorithm; section 3 introduces the finite element model; section 4 presents the dimensional analysis to identify the relevant parameters to be investigated, the model parameter identification, the validation and an additional parametric study; and, finally, section 5 discusses the origin of the parameter effects and the limits of the selected failure criterion. Beyond the novel and useful results in the scope of electronic assembly solder joints, the originality of this study is to set a methodology that combines a machine learning approach to treat a wide set of experimental data and to validate an advanced thermomechanical model.

2. Experimental data processing

The experimental data are based on micro-sections performed on different resistor sizes, mounting processes, joint thickness and termination lengths observed by microscopy. These samples were exposed to 500 thermal cycles as defined in Figure 1 (-55/+100°C, 10°C/min and 15min dwell time, following the ECSS Q-ST-70-61C [17] standard). The available data are processed through a machine learning approach in order to compare and validate the numerical results.

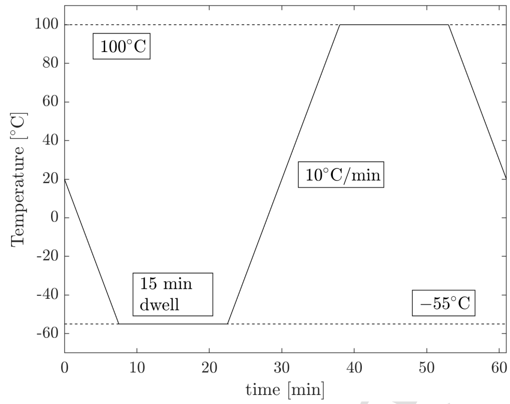

Figure 1: Thermal cycle applied experimentally and to the FE model according to the standard ECSS-Q-ST-70-61C [17].

2.1. Experimental methods

A typical surface-mounted resistor soldered on a PCB is presented in Figure 2 and a micro-computed tomography image of this assembly is also included. The resistive layer and both solder joints can be identified on the PCB. The latter is only visible through the copper paths and planes, with the fiber-reinforced polyimide matrix being X-ray transparent. The ceramic substrate (e.g. alumina) does not appear in the micrograph. The cutting plane corresponding to the micro-sectioning is also highlighted. The solder material is a tin-lead alloy 62Sn (62 % of tin, 36 % of lead and 2% of silver).

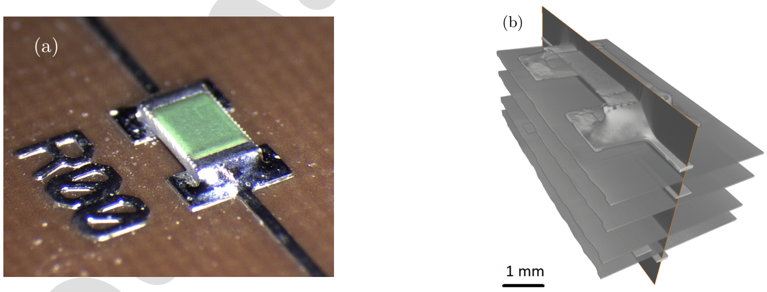

Figure 2: Configuration of an electronic component assembly: (a) surface-mounted resistor soldered on a PCB and (b) micro-computed tomography of the assembly. The vertical dark grey plane corresponds to the micro-section cutting plane.

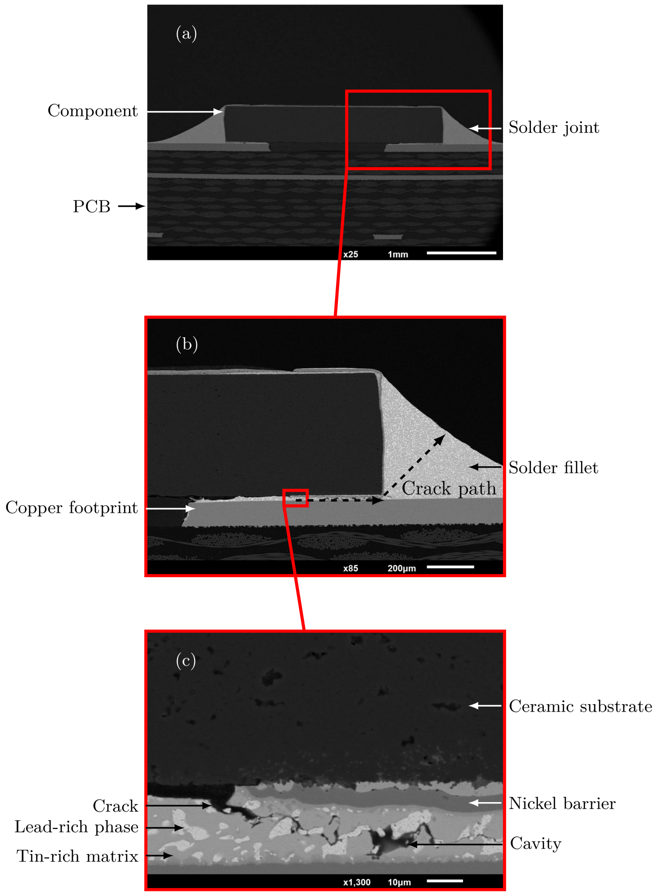

Figure 3: SEM micrograph of a ceramic resistor assembly micro-section with (a) a global view, (b) a focus on one joint and (c) a magnification of the onset region of the crack, underneath the component.

Scanning electron microscopy (SEM) is used to characterize cross-sections of thermally aged components. Figure 3 shows three magnifications of a typical surface-mounted resistor assembly. The crack initiates underneath the component, close to the tip of the nickel barrier (left side of Figure 3c) and propagates towards the termination corner (on the right side of Figure 3b), and finally, complete failure is achieved when the solder filet is cracked. Particular attention is paid to the crack initiation region, i.e. underneath the component. In what follows, the crack length is defined in terms of percentage relative to the length of this initiation region, meaning that a length of more than 100 % is required to lead to complete failure, including the solder fillet region. The heterogeneity of the solder material can be observed in Figure 3c, with lead-rich inclusions embedded within a tin-rich matrix.

A first set of experimental results comprises data of 139 joints (i.e. 80% of the 174 joints included in this study) and is used to train the machine learning model. The 35 remaining solder joints are part of the test set to assess the model predictions. Joints are randomly distributed between both sets. More than twenty trainings have been performed to ensure that there is no significant dependency on subset selection. They contain the following information: joint thickness, component length and thickness, termination length and crack length at 500 cycles. Resistor packages belong to five size classes, 0402, 0603, 0805, 1206 and 2010 with 16, 50, 56, 46 and 6 samples that belong to each class, respectively. The first two figures indicate the component length and the last two the component width, both expressed in hundredths of inches. Both training and test sets cover the entire range of component sizes and close to the entire range of solder joint thicknesses. Figure 4 shows the distribution of the crack lengths extracted from the solder joint database. One may notice the rather binary distribution, partially cracked samples are scarce.

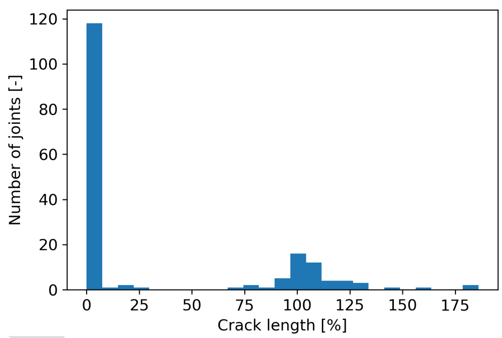

Figure 4: Distribution of measured crack lengths at 500 cycles for surface-mounted resistors extracted from the database.

2.2. *Machine learning data processing*

The machine learning platform Tensorflow and Keras API [18] are used. The machine learning model is divided into two submodels. The first submodel is a classification which categorizes if a joint is cracked or not and the second is a regression that provides the crack length. Both submodels are fully connected neural networks. The classification uses the rectified linear activation function and two hidden layers (consisting of 5 and 3 neurons) with a binary cross entropy loss function. The probability to be cracked is generated by the softmax function [19]. The classification outputs are rounded to produce a value of 0 for non-cracked and 1 for cracked joints and set as an additional parameter for the second submodel by adding this parameter in the regression input layer. This submodel consists of three hidden layers (including 4, 3 and 2 neurons), uses the hyperbolic tangent activation function and the mean squared error loss function. The classification allows the regression to be more accurate, essentially centered around 0% cracked and 100% cracked joints (see Figure 4).

A comparison between the classification submodel predictions and the 35 joints of the test data set is presented in Figure 5 in terms of normalized crack length. Three predictions of the test set were incorrect, leading to an overall accuracy of about 90 %. It is extremely difficult to improve the accuracy with the available data. Very similar configurations (resistor size, solder joint thickness) can sometimes lead to apparently conflicting results. Other parameters, not taken into account in the database, influence the sensitivity to cracking. These parameters, including component tilt and alignment and/or the presence of voids (size, distribution), are often difficult to characterize and control.

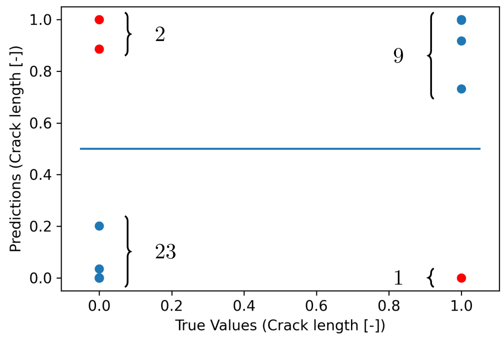

Figure 5: Prediction assessment of the classification submodel; true values refer to experimentally measured cracked or uncracked samples and predictions to the classification estimates based on the 35 joints that are part of the test set. The number of samples that belong to each class is also indicated (some points overlap). The 3 incorrect predictions are highlighted in red.

Predictions and measured true values of the test set can now be compared to evaluate the accuracy of the regression submodel. Figure 6a shows that three predictions (two at 100% and one at 0%) are incorrect. The latter can be attributed to the incorrect classification of the first submodel, see Figure 5. Regions around 0 and 100 % crack lengths are readily identified. The important conclusion emerging from this analysis is that when failure starts, the crack rapidly propagates throughout the joint underneath the component. In other words, the incubation/initiation stage must be captured accurately by the thermomechanical model for accurate failure assessment in the scope of the present study.

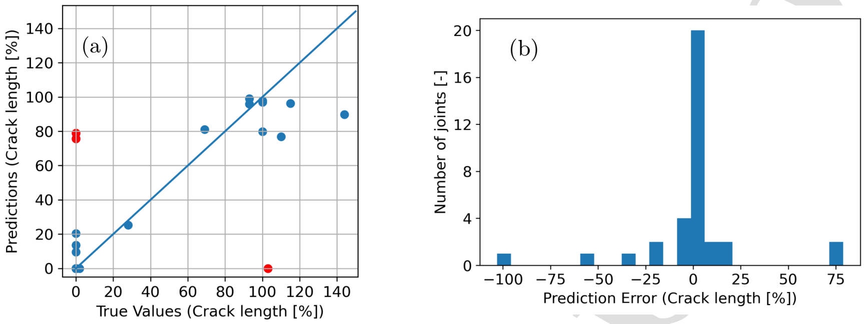

Figure 6: Prediction assessment of the regression submodel with (a) a comparison between experimentally observed true crack lengths and model predictions (misclassified samples are shown in red, see Figure 5) and (b) the distribution of the predictions errors.

Prediction errors are presented in the histogram of Figure 6b; 85 % of predicted crack lengths (30 out of 35 joints) are within plus or minus 25 % of true values. Only the three misclassified predictions have errors larger than 60 %. This analysis proves an overall good accuracy and sets a fair basis for validating the finite element model (section 3).

The effect of solder joint thickness on reliability is now investigated for several resistor sizes. The predicted crack lengths extracted from the machine learning model are shown in Figure 7 as a function of the solder joint thickness normalized by the PCB thickness. Due to the lack of available data for the largest and the smallest component sizes (i.e. 2010 and 0402), predictions must be considered with care; especially for the 2010 resistors with a normalized solder joint thickness (t_{solder}/t_{PCB}) larger than $10 \cdot 10^{-3}$. The component size has a major impact on reliability with increasing crack lengths for larger components. A significant change of behaviour, between thin and thick joints is clearly observed for the 0805 and 1206 sizes, indicating that thinner joints are much more prone to cracking. This example illustrates the interpolation capabilities offered by the machine learning approach and related opportunities for comparisons with numerical predictions.

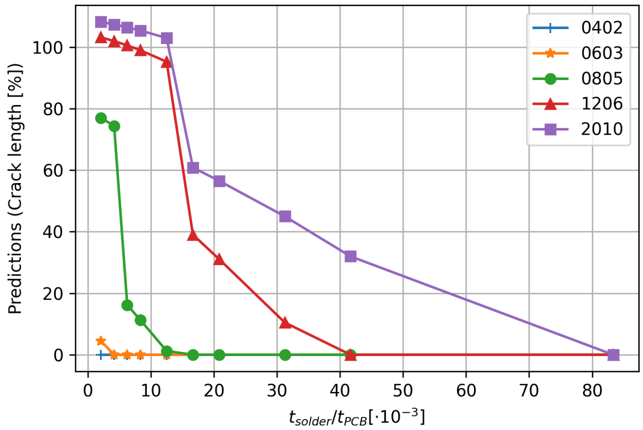

Figure 7: Impact of the joint thickness normalized by the PCB thickness on the predicted crack lengths for several resistor sizes. The component nomenclature used in the legend is as follows: the first two figures indicate the component length and the last two, the component width, both expressed in hundredths of inches.

3. Finite element model

The finite element (FE) model is described in this section including the geometry and meshing, the material's constitutive behaviours, the cohesive zone description and the loading conditions. The implicit solver of the Abaqus finite element software [20] is used.

3.1. Geometry of the assembly

The component is a surface-mounted ceramic resistor with nickel terminations mounted on a copper footprint, part of a printed circuit board as shown in Figure 8. Alumina (Al_2O_3) is considered as component ceramic body. The PCB material is polyimide Arlon 35N [21]. Two-dimensional plane strain conditions are imposed, justified by the observation that the out-of-plane width is much larger than the thickness of the layers undergoing the failure process. This assumption, although fully valid for to the near crack tip zone where failure occurs, introduces differences with respect to the true problem in terms of the generation of the thermal strain components which is essentially equibiaxial. For instance, the actual out-of-plane width of the component body is much smaller than the PCB width. It brings in a small bias on absolute crack length values.

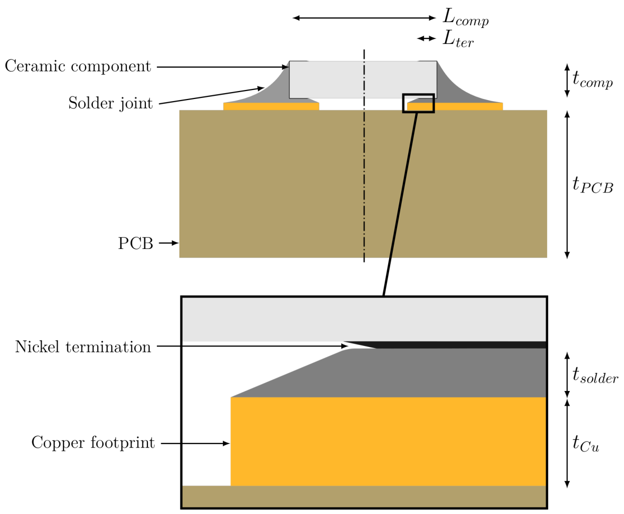

Figure 8: Model geometry with a magnified view of the crack initiation region underneath the component.

The FE mesh is presented in Figure 9. A zoom on the region underneath the component is also provided. The interface between the nickel barrier and the solder joint is highlighted in red and corresponds to the region where the cohesive zone is inserted. A characteristic mesh length of 0.9% of the termination length has been set at this interface. It corresponds to 112 cohesive elements distributed from the initial crack tip to the end of the region underneath the component, i.e. up to the fillet of the joint. The element size of the cohesive zone as well as of the layers above and below is kept constant throughout this study.

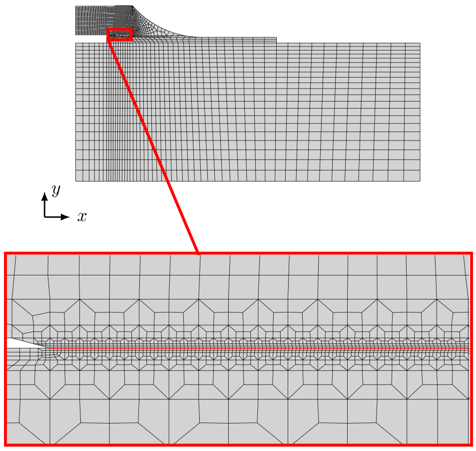

Figure 9: Mesh of the FE model with a magnification of the crack propagation region showing the cohesive zone highlighted in red.

The component assembly is subjected to the thermal cycle shown in Figure 1. The temperature is imposed to be uniform within the model owing to the small size of the ceramic component. Note that the model is sensitive to time (see Equation 1) and thus to the heating rate.

3.2. Description of the materials

3.2.1. Material behaviour

All materials are considered thermally isotropic with a coefficient of thermal expansion α. Linear elastic isotropic behaviour is assumed for all materials with Young's modulus E and Poisson ratio ν, via Hooke's law.

Plastic deformation is allowed in both nickel and copper materials according to experimental data from Jenkins *et al.* [22] and modelled using J_2 flow theory. The temperature-dependent viscoplastic behaviour of the solder alloy is described using Anand's model [23]. Other models have been studied in the literature, some of them considering grain size effects [24].

$$\dot{\epsilon}^p = A \exp\left(\frac{-Q}{RT}\right)\left[\sinh\left(\xi \frac{\sigma}{s}\right)\right]^{1/m}, \tag{1}$$

where

$\dot{\epsilon}^p$ is the inelastic strain rate,
A is a material constant,
ξ is the stress multiplier,
m is the strain rate sensitivity,
Q is the activation energy,
R is the ideal gas constant,
s is the deformation resistance which is computed via an evolution law:

$$\dot{s} = h_0 \big| 1 - \frac{s}{s^*} \big|^a \mathrm{sign}\big(1 - \frac{s}{s^*}\big) \dot{\epsilon}^p, \tag{2}$$

where
h_0 is the hardening constant,
a is the hardening strain rate sensitivity,
s^* is the saturation value of s, which writes:

$$s^* = \hat{s} \Big[\frac{\dot{\epsilon}^p}{A} \exp\big(\frac{Q}{RT}\big) \Big]^n, \tag{3}$$

where
$\hat{s}$ is a coefficient of the saturation of the deformation resistance,
n is the strain rate sensitivity of the saturation of the deformation resistance.

The initial value of the deformation resistance, s_0, is also a material parameter.

3.2.2. Material parameters

Table 1 and 2 list the values of the material parameters extracted from literature [3, 6, 16, 25, 26]. The Young's modulus and reference stress values are normalized by the initial yield stress of the solder joint σ_{y0}, equal to 28 MPa (at 20°C and at an inelastic strain rate of $5 \cdot 10^{-4}$ [s^{-1}]), calculated from Anand's model parameters [6]. As suggested by Basaran and Jiang [27], the Young's modulus of the solder alloy has been measured by nano-indentation on an actual manufactured sample, confirming the value of 42 GPa (at 25 °C) computed from the temperature-dependent equation in Table 1.

Table 1: Elastic properties and coefficients of thermal expansion, from [3, 25, 26, 16].

Material	E [GPa]	E/σ_{y0} $[-]$	ν $[-]$	α $[10^{-6}\cdot°C^{-1}]$
Alumina ceramic	410	14 640	0.25	5.5
Nickel	180	6430	0.31	13
Solder	$62 - 0.067\cdot T$	$2214 - 2.39\cdot T$	0.35	27
Copper	120	4290	0.35	17
Polyimide PCB	27	964	0.3	15.5

Table 2: The values of Anand's parameters for 62Sn36Pb2Ag solder alloy, according to Darveaux [6].

Material parameter	value	dimensionless value $[-]$
A	$4 \cdot 10^6$ $[s^{-1}]$	-
Q/R	9400 [K]	-
ξ	1.5 [-]	-
m	0.303 [-]	-
h_0	1379 [MPa]	49.25
a	1.3 [-]	-
$\hat{s}$	13.79 [MPa]	0.4925
n	0.07 [-]	-
s_0	12.41 [MPa]	0.4432

3.3. Cohesive zone model (CZM)

3.3.1. Model description

A layer of zero-thickness cohesive elements is inserted at the interface between the solder joint and the horizontal interface of the component, just below the nickel layer, see Figure 9.

A bi-linear (triangular) traction-separation law represents the near interface behaviour under traction and shear forces, see Figure 10, with a peak stress $\hat{\sigma}$ and a fracture energy Γ_0. The separation is normalized by the thickness of a selected thick joint of 200 μm. The unloading/reloading behaviour is also displayed in Figure 10. The initial stiffness of the traction-separation law is chosen sufficiently high to avoid adding non-physical compliance to the system; it is raised to 1000 times the elastic modulus of the solder at 20°C, in both normal and shear directions. For convenience, peak stresses and fracture energies are equal for both mode I and mode II. Only traction is considered in mode I conditions, compression does not impact the cohesive behaviour. Mixed-mode damage initiation occurs when the following criterion is met [20]:

$$\left(\frac{\langle t_n \rangle}{t_n^0}\right)^2 + \left(\frac{t_s}{t_s^0}\right)^2 = 1, \tag{4}$$

where

$\langle t_n \rangle$ and t_s are the traction and shear stresses, respectively,
t_n^0 and t_s^0 are the peak traction and shear stresses, respectively.

The peak stress and the fracture energy are temperature-dependent. The peak stress follows the evolution with the temperature of the initial yield stress of bulk solder at a strain rate of 10^{-3} [s^{-1}]. The fracture energy decreases with temperature to keep the critical separation δ_c constant with temperature. It leads to a fracture energy divided by almost 2 when going from -55 to 20°C (see Figure 10). This assumption is in line with the experimental results obtained by Logsdon *et al.* [28], who found a fracture toughness of 329 and 165 kJ/m^2 at -55 and 24°C, respectively.

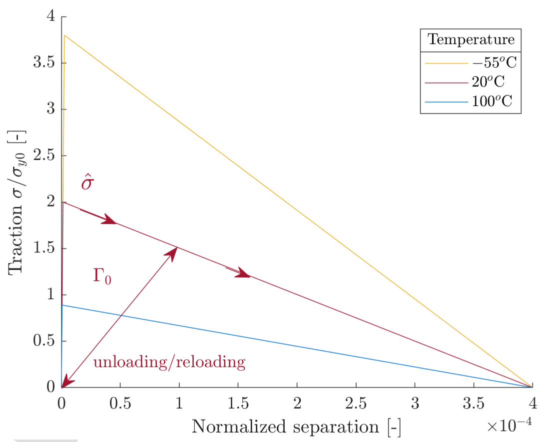

Figure 10: Temperature-dependent traction-separation law applied to cohesive elements.

3.3.2. Selection of the fracture energy value

The selection of physical values or bounds for Γ_0 is not a trivial issue. The total fracture energy during crack propagation can be written as the sum of a fracture energy Γ_0 and a plastic dissipation Γ_p:

$$\Gamma_c = \Gamma_0 + \Gamma_p. \tag{5}$$

In brittle materials and interfaces, Γ_0 tends toward two times the surface energy, but it can be significantly larger if plasticity and damage mechanisms develop in the fracture process zone leading to important dissipation and toughening. Experimental measurements have been reported in literature for both bulk [28] and finite thickness joint [29, 30] conditions, see Table 3. The fracture energy is extremely dependent on the thickness of the joint. This suggests that the remote plastic dissipation Γ_p can be orders of magnitude larger than Γ_0, especially for thick joints and bulk material samples [31].

Table 3: Experimental fracture energy, from [28, 29, 30].

Joint thickness	76 [μm]	254 [μm]	bulk
G_c[J/m^2]	≈ 60	≈ 1400	$\approx 165{,}000$

For metals such as lead, the surface energy is equal to 0.5 J/m^2 [32], such that $\Gamma_0|_{min}$ is of the order of 1 J/m^2. This value is the minimum value of Γ_0 considered in our numerical simulations. And, from the measured toughness of the thinnest joint (Table 3), an upper bound of Γ_0 can be set at 60 J/m^2.

As a first-order approximation, one can estimate the radius of the plastic zone size according to Irwin's criterion [33]:

$$r_p = \frac{E_{solder}\Gamma_0}{3\pi(1-\nu_{solder}^2)s_0^2} \approx 6 \text{ to } 390 \text{ } [\mu\text{m}]. \tag{6}$$

The plastic zone size is within the range of typical joint thickness. This is also common for adhesive joints [34, 35, 36]. The limited joint thickness imposes a constraint on the expansion of the plastic zone. Hence, the Γ_p term increases with thickness until a threshold, before tending to the small scale yielding value which is often smaller than the maximum Γ_p attained at an intermediate thickness [34, 35, 37].

3.3.3. Selection of the peak stress value

The peak stress value directly controls plastic dissipation throughout the joint. Most simulations are performed with a constant normalized peak stress ($\hat{\sigma}/\sigma_{y0}$) of 2 (at 20°C), see Figure 10. Numerous convergence issues have been encountered with lower values, e.g. $\hat{\sigma}/\sigma_{y0} = 1$ (at 20°C). Such a low value leads to the emergence of a second failure process zone at the other end of the joint (see right-hand side of the cohesive zone in Figure 9). This is usually not observed during experimental tests, justifying the use of a normalized peak stress larger than 1.

4. Model validation and parametric study

A dimensional analysis is first performed to identify the relevant non-dimensional parameters to guide the parametric survey. The numerical model parameters are then identified and validated by comparison with the machine learning processed experimental data. An additional parametric study is finally proposed outside of the available data set.

4.1. Dimensional analysis

The main focus of the parametric study is on the role of geometric dimensions on the predicted failure response. The dimensions of interest were shown in Figure 8, including the component length L_{comp}, thickness t_{comp}, termination length L_{ter}, solder joint thickness t_{solder} and copper footprint thickness t_{Cu}. The PCB thickness (t_{PCB}) is selected as a reference length.

The lifetime of the assembly is assessed through a failure criterion F. It is expressed as a function of the most relevant parameters (see Figure 8):

$$F = f\left(\frac{E_{solder}\Gamma_0}{3\pi(1-\nu_{solder}^2)s_0^2 t_{solder}}, \frac{t_{solder}}{t_{PCB}}, \frac{t_{Cu}}{t_{PCB}}, \frac{t_{comp}}{t_{PCB}}, \frac{L_{comp}}{t_{PCB}}, \frac{L_{ter}}{t_{PCB}}, \frac{E_{PCB}}{E_{solder}}\right). \tag{7}$$

In this study, after several preliminary investigations, failure is defined based on the crack length after 100 thermal cycles; this will be explained in more detail later in this section. The relative crack length is expressed in percent of the interface length between the component termination and the solder joint; in other words, the crack length a is normalized by L_{ter} (see Figure 8). Figure 11 illustrates an example of a simulated crack length.

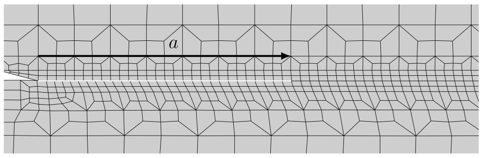

Figure 11: Simulated crack length a. The crack is highlighted in white and the growth direction is depicted with a black arrow.

Figure 12 shows the variation of the relative crack length as a function of the number of cycles for several preliminary simulations, for several component length and thickness configurations. The crack growth rates are not constant during crack propagation. Thick and large configurations exhibit accelerated crack growth before complete failure whereas saturation is observed for the shortest component. The crack growth rate can initially be high to decrease to moderate levels at increased number of cycles, see e.g. $L_{comp}/t_{PCB} = 1.2$ in Figure 12a. This behaviour motivates the use of the proposed crack length indicator after 100 cycles instead of a crack growth rate indicator such as $\mathrm{da/dN}|_{\mathrm{init}}$. Full failure can also be attained before 100 cycles. Sometimes, numerical instabilities do not allow simulations to run until complete failure.

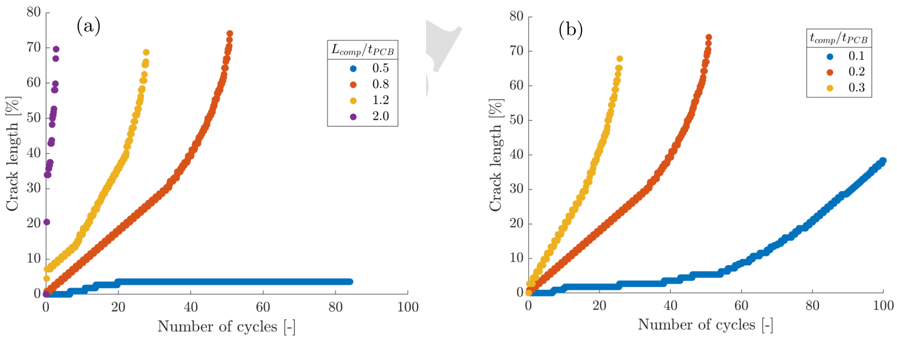

Figure 12: Determination of an appropriate failure criterion based on a series of preliminary simulations showing the variation of crack length with the number of cycles for several component (a) lengths (L_{comp}/t_{PCB}) and (b) thicknesses (t_{comp}/t_{PCB}).

A systematic analysis of the complete failure of the joint (100% of the termination length) was not attempted to reduce the computational burden in addition to convergence issues. The number of cycles could have been increased up to 500 as well to allow one-to-one comparisons with experimental data but, again, it would have significantly increased computational costs. A trade-off was thus selected at 100 cycles.

Most simulations are carried out in a finite strain setting. However, in order to overcome possible convergence difficulties already mentioned above, some simulations were conducted within a small strain framework. A comparison between finite strain and small strain predictions for selected simulation cases is included in Appendix A. Results obtained with a small strain setting will be marked by a '+' sign in subsequent Figures 13 and 14. In the following parametric study, unless otherwise specified, the set of dimensionless parameters is given in Table 4.

Table 4: Default dimensionless parameters used in the parametric study.

L_{comp}/t_{PCB}	t_{comp}/t_{PCB}	t_{solder}/t_{PCB}	L_{ter}/t_{PCB}	t_{Cu}/t_{PCB}	E_{PCB}/E_{solder}
0.8	0.2	0.015	0.13	0.04	0.64

4.2. Identification of Γ_0

The identification of the fracture energy value is performed through the analysis of the effect of both component length L_{comp} and thickness t_{comp}. Figure 13 shows the variation of the crack lengths after 100 cycles as a function of the component length for different thicknesses and for three values of Γ_0: (a) 1, (b) 2 and (c) 4 J/m^2 (at 20°C). The machine learning processed experimental data (dotted lines) are compared to numerical results (solid lines). Due to convergence issues, it has not been possible to obtain the simulated crack length for $\Gamma_0 = 2$ J/m^2 (Figure 13b) at $L_{comp}/t_{PCB} = 2$ for the thinnest component and to overcome the missing value, another simulation with a shorter component has been conducted.

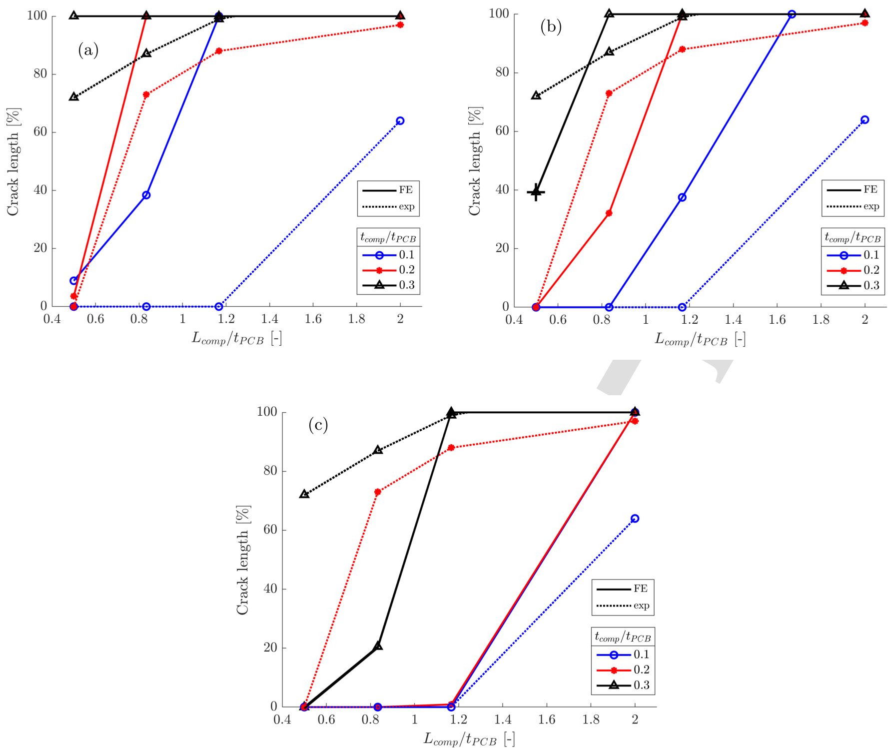

Figure 13: Effect of L_{comp}/t_{PCB} and t_{comp}/t_{PCB} on crack lengths for FE simulations with (a) $\Gamma_0 = 1$ J/m^2, (b) $\Gamma_0 = 2$ J/m^2 and (c) $\Gamma_0 = 4$ J/m^2 (at 20°C) and machine learning processed experimental data. A '+' sign indicates a simulation performed under a small strain framework (Appendix A).

First, the FE model adequately captures the experimental trend predicted by the machine learning analysis of Section 2.2. These results show that both the length and the thickness of components have a first-order effect on the crack lengths. Longer and thicker joints are more prone to cracking than short and thin configurations. With $\Gamma_0 = 1$ J/m^2, the predicted crack lengths are in line with the machine learning processed experimental data for the two thickest components. However, the trend for the thinnest component diverges from the micro-section observations, significantly overestimating the crack length. For $\Gamma_0 = 4$ J/m^2, the behaviour of the thinnest component is well captured but for both normalized thicknesses $t_{comp}/t_{PCB} = 0.2$ and 0.3, the numerical results underestimate the crack length. The intermediate work of separation value $\Gamma_0 = 2$ J/m^2 provides the best predictions and will be selected in what follows unless explicitly mentioned otherwise. Both machine learning and numerical trends are close, from a qualitative point of view but also quantitatively. This is a major result of this work made possible by the use of the machine learning approach to extract the trends needed for model comparison and validation.

4.3. Validation

4.3.1. Effect of solder joint thickness t_{solder}

The magnitude of the solder thickness significantly impacts the failure resistance according to observations and experience, see Figure 7. In general, the thicker the joint, the longer the lifetime. Simulations have been conducted for the three works of separation values $\Gamma_0 = 1$, 2 and 4 J/m^2. The comparison between the numerical and machine learning predicted crack lengths is shown in Figure 14. For $\Gamma_0 = 2$ and 4 J/m^2, a minimum crack length is obtained at an intermediate solder joint thickness (around a thickness ratio of $40 \cdot 10^{-3}$ for $\Gamma_0 = 2$ J/m^2 and between 10 and $40 \cdot 10^{-3}$ for $\Gamma_0 = 4$ J/m^2). Experimentally, this is not observed on micro-sections but, generally, the solder joint thickness rarely exceeds $t_{solder}/t_{PCB} = 40 \cdot 10^{-3}$ and no data was available above $t_{solder}/t_{PCB} = 100 \cdot 10^{-3}$ to confirm this trend. Note that these results confirm, similarly to Figure 13, that $\Gamma_0 = 2$ J/m^2 provides the best crack length predictions and reasonably well describes the experimental observations. The model correctly captures the crack resistance up to a normalized thickness of $40 \cdot 10^{-3}$ while overestimating the crack growth rate.

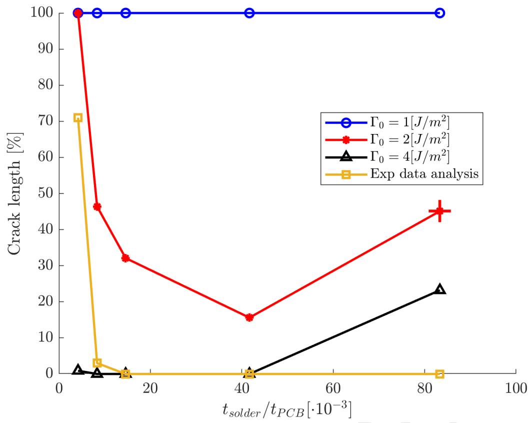

Figure 14: Effect of t_{solder}/t_{PCB} on crack lengths for FE simulations with $\Gamma_0 = 1$, 2 and 4 J/m^2 (at 20°C) and machine learning processed experimental data. A '+' sign indicates the simulation performed under a small strain framework (Appendix A).

4.3.2. Effect of component termination length L_{ter}

The termination length of the component is also the contact length between the solder joint and the bottom of the component and hence, the length of the cohesive zone. Numerical results presented from this section are simulated with the previously selected work of separation $\Gamma_0 = 2$ J/m^2. Figure 15 indicates that the termination length is also a first-order parameter affecting fatigue failure resistance. Within the simulated length range, the crack length varies from around 100 % down to 0 %, for short and long terminations, respectively. The impact is also more pronounced between the two shortest lengths than for the others. The trend captured by the finite element model qualitatively and quantitatively agrees with the experimental micro-section characterizations.

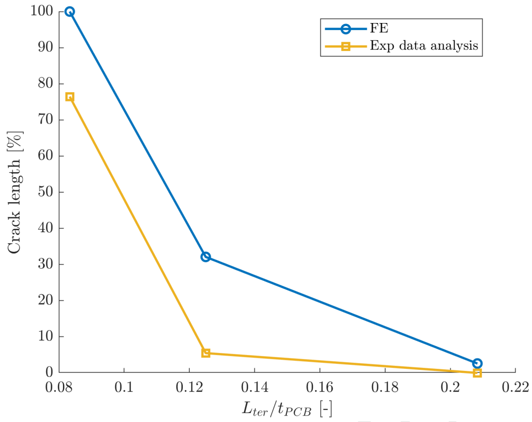

Figure 15: Effect of L_{ter}/t_{PCB} on crack lengths for FE simulations and machine learning processed experimental data.

4.4. Additional parametric study

The role of two additional parameters on joint failure, i.e. the copper pad thickness and the PCB stiffness, that were not part of the experimental database and hence not part of the machine learning approach, is now explored in this section.

4.4.1. Effect of copper pad thickness t_{Cu}

The copper pad thickness t_{Cu} (see Figure 8) is another parameter that can vary in actual printed circuit boards. Several configurations are simulated for a range of t_{Cu}/t_{PCB} varying between $4 \cdot 10^{-3}$ and $63 \cdot 10^{-3}$. This range of normalized copper pad thickness is wider than in practice, where t_{Cu}/t_{PCB} is often close to $30 \cdot 10^{-3}$. Figure 16a shows that an increase in the copper pad thickness significantly delays crack propagation.

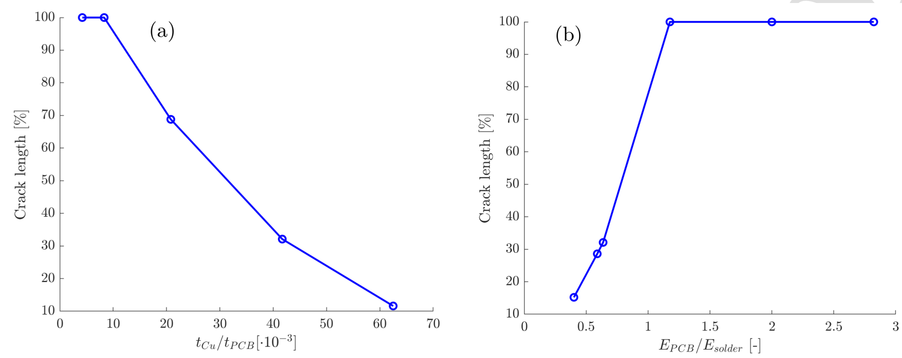

Figure 16: Additional parametric study on (a) the effect of t_{Cu}/t_{PCB} and (b) the effect of E_{PCB}/E_{solder} on the FE model predicted crack lengths.

4.4.2. Effect of PCB elastic modulus E_{PCB}

The PCB copper content influences the apparent elastic modulus as copper is much stiffer than glass fiber reinforced polyimide. Fabric and resin volume fractions are also important parameters and can significantly impact the material properties [38]. The elastic modulus is varied from glass fiber reinforced epoxy PCB material without copper, i.e. 17 GPa [39], polyimide also without copper, i.e. 25 GPa [21] (the two lowest values) to pure copper, the highest modulus with 120 GPa [40]. In this very broad range of E_{PCB}/E_{solder}, a significant impact on crack resistance is predicted, see Figure 16b. Increasing the PCB stiffness results in joints being more susceptible to fatigue cracking. This may be explained by the increase of the overall stiffness of the assembly, the joint being more constrained during thermal cycles.

5. Discussion

5.1. Origin of the parameter effects

To supplement and further discuss the crack propagation behaviour, it is insightful to address a more simple static analysis (without CZM) in order to unravel the fundamental origin of the different effects discussed up to now by looking at the field quantities. In particular, emphasis will be placed on the role of equivalent inelastic strain per cycle (ϵ_{eq}^{in}/cycle) at the crack tip (left-hand side of the magnification presented in Figure 9), which is also the location where the inelastic strains are the largest. Figure 17 shows this maximum ϵ_{eq}^{in} for (a) several component lengths and (b) several solder joint thicknesses. The amount of inelastic strain accumulated is higher when the component length increases, leading to premature damage of the joint. This is in line with the longer cracks predicted by the crack propagation simulations, see Figure 13b. The accumulated inelastic strain decreases with solder joint thickness (Figure 17b) until a normalized joint thickness of around 40 [-], from which it starts to increase. Again, this behaviour is similar to the crack propagation analysis presented in Figure 14.

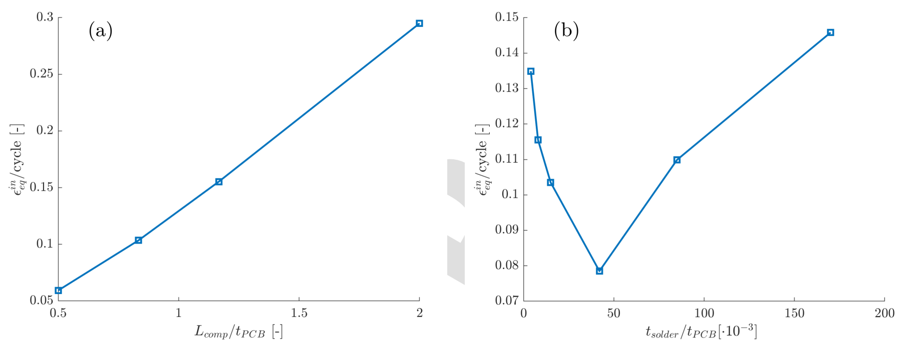

Figure 17: Equivalent inelastic strain generated per cycle at the crack tip for several (a) component lengths and (b) solder joint thicknesses during a static analysis (i.e. without crack propagation).

This comparison is now extended to configurations previously simulated in Section 4. Figure 18 presents both static (with the accumulated inelastic strain per cycle at the crack tip as a failure criterion) and propagation (with crack lengths after 100 thermal cycles) approaches. The trend of Figure 17 is confirmed. However, a static analysis does not have the level of richness of the crack propagation studies on thermal ageing behaviour. The crack growth behaviour can, indeed, reveal self stabilizing effects (see $t_{solder}/t_{PCB} = 85 \cdot 10^{-3}$ in Figure 20) or unstable crack growth (see $t_{solder}/t_{PCB} = 4 \cdot 10^{-3}$), leading to an accelerated failure. This will be discussed in section 5.2.

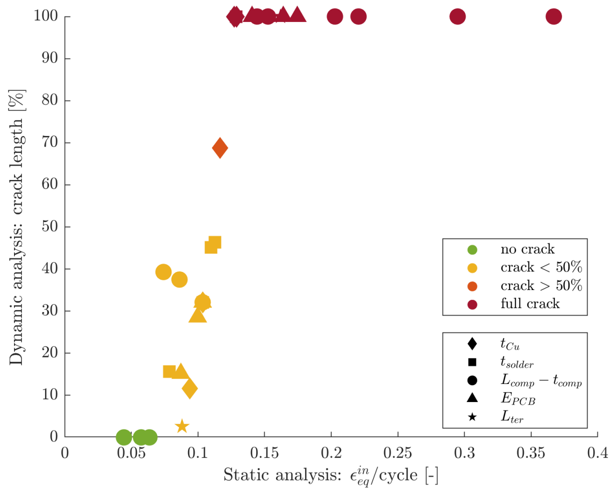

Figure 18: Comparison between the crack length failure criterion (with the identified fracture energy $\Gamma_0 = 2$ J/m^2) and the inelastic strain accumulated per cycle at the crack tip (static analysis) for every simulation presented in the previous section. The symbols represent the various parameters investigated.

5.2. Relative importance of shear and tensile stress components

The FE model also allows the identification of the distribution between shear and normal stress components. The evolution of the ratio of shear and tensile stress ranges during the hundredth cycle can be investigated for several conditions. Figure 19 shows the variation of this stress ratio in a static analysis for the simulated range of normalized copper footprint thickness and PCB stiffness. An increase of t_{Cu}/t_{PCB} causes an increase in shear stresses relative to tensile stresses. It also highlights, as expected, that shear is the prevailing component responsible for solder joint failure. Increasing PCB stiffness leads to a decrease in the shear to traction ratio up to a point where the normal stress slightly dominates the shear component.

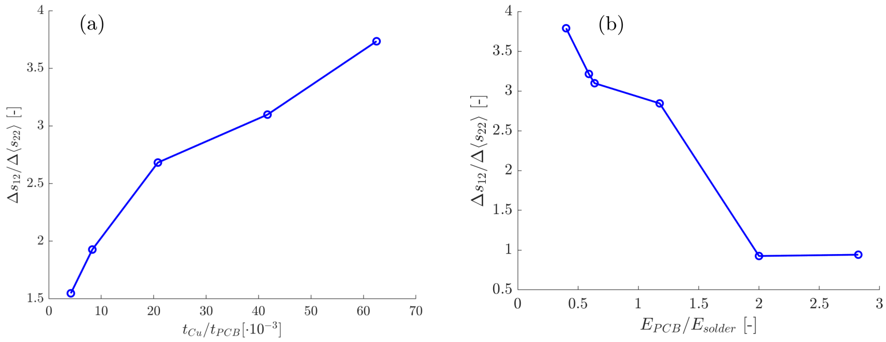

Figure 19: Relative importance of shear and tensile stress ranges during the hundredth thermal cycle at the crack tip for several (a) copper footprint thicknesses and (b) PCB stiffnesses during a static analysis.

5.3. Limits and perspectives of the selected failure criterion

As already discussed in Section 4.1, the selection of a failure criterion is a trade-off between computational cost, possible convergence issues and representativeness. Figure 20 presents the variation of the crack length as a function of the number of thermal cycles for four normalized joint thicknesses ranging from 4 to $85 \cdot 10^{-3}$. For a thin joint, i.e. $t_{solder}/t_{PCB} = 4 \cdot 10^{-3}$, the crack growth rate is relatively constant up to 40 to 50 cycles, where it starts to increase. The propagation then accelerates until complete failure. For thicker joints, after a first propagation stage, the crack growth rate decreases significantly (for $t_{solder}/t_{PCB} = 15 \cdot 10^{-3}$ and $42 \cdot 10^{-3}$), up to a plateau (for $t_{solder}/t_{PCB} = 85 \cdot 10^{-3}$). This first propagation stage is amplified for thicker joints, see especially $t_{solder}/t_{PCB} = 42 \cdot 10^{-3}$ and $t_{solder}/t_{PCB} = 85 \cdot 10^{-3}$. After the low crack growth rate stage, it increases again, see $t_{solder}/t_{PCB} = 15 \cdot 10^{-3}$. These highly non-uniform and non-linear behaviours highlight the limitation of the selected failure criterion at 100 cycles. Still, the cohesive zone model has been validated and showed its ability to predict crack lengths in accordance with the machine learning processed experimental data. As a perspective, more sophisticated failure criteria related to the crack propagation behaviour, such as the crack growth rate, could therefore provide additional insight to this analysis. Grain size effects on solder material behaviour could also be investigated to better link with material characteristics and probably enhance even more the predictive capabilities of the model.

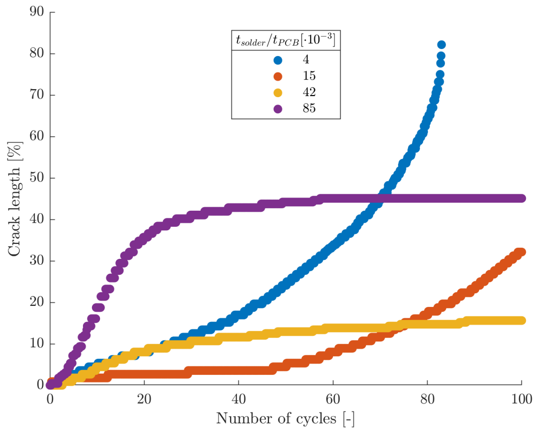

Figure 20: Variation of the crack length as a function of the number of cycles predicted by the FE model for several joint thicknesses.

6. Conclusions

An advanced finite element model predicts the fatigue crack propagation in electronic component solder joints subjected to cyclic thermal loading, accounting for the viscoplastic behaviour of the joint and the failure process for a wide range of assembly configurations. Comparisons between FE simulations and machine learning processed experimental data were conducted and showed the ability of the selected cohesive zone model to adequately capture the experimentally observed trends. The main findings of this study are:

- Machine learning techniques facilitate data analysis of micro-section damage observations and provide rationalization of the effect of individual assembly parameters on solder joint failure. This innovative data treatment improves the relevance of the validation of the numerical model and leads to more exploitable results.

- A finite element model is constructed accounting for (i) the temperature-dependent viscoplastic constitutive behaviour of the solder material and (ii) the fatigue crack nucleation and growth via a traction-separation law. The fatigue crack growth predictions are in agreement with the machine learning processed experimental observations.

- Geometric properties such as component length, thickness, termination length, copper pad and solder joint thickness, as well as PCB stiffness, considerably influence the crack growth rate and therefore assembly reliability.
- Predictions based on the accumulated inelastic strain per cycle as a failure criterion (obtained via simplified static finite element calculations without crack nucleation and growth) are in line with those obtained with more sophisticated crack growth simulations but do not provide insight on the role of assembly parameters on crack growth.
- An increase of the shear stress component driving the growth of the fatigue crack is found when increasing the copper pad thickness and decreasing the PCB stiffness.

The present study provides design guidelines for new or optimized assemblies with respect to thermomechanical reliability. These considerations can also help to predict damage accumulation on existing component assemblies. In summary, based on the explored parameter space in this study, the following configurations lead to an increased resistance to joint failure: (i) a short and thin component, (ii) a sufficiently thick joint, (iii) a long component termination, (iv) a thick PCB copper pad, and (v) a low PCB elastic modulus.

Acknowledgements

We thank the Service Public de Wallonie-Wallonie recherche for financial support through the project "Stress", Dr. Grzegorz Pyka for providing support on micro-computed tomography, Dr. Ingo Scheider for his precious help to obtain converging and reliable numerical simulations and Dr. Marc Bekemans and Dr. Benoît Dompierre for inspiring discussions. Computational resources have been provided by the supercomputing facilities of the Université catholique de Louvain (CISM/UCL) and the Consortium des Équipements de Calcul Intensif en Fédération Wallonie Bruxelles (CÉCI) funded by the Fond de la Recherche Scientifique de Belgique (F.R.S.-FNRS) under convention 2.5020.11 and by the Walloon Region.

Code availability

The code will be made available to reader upon reasonable request.

Appendix A. Small strain and finite strain frameworks

Due to convergence issues, several simulations were conducted with a small strain instead of a finite strain setting. Figure A.21 shows two comparisons between these two frameworks. It only slightly impacts crack lengths and allows more calculations to run, such as illustrated in Figure A.22.

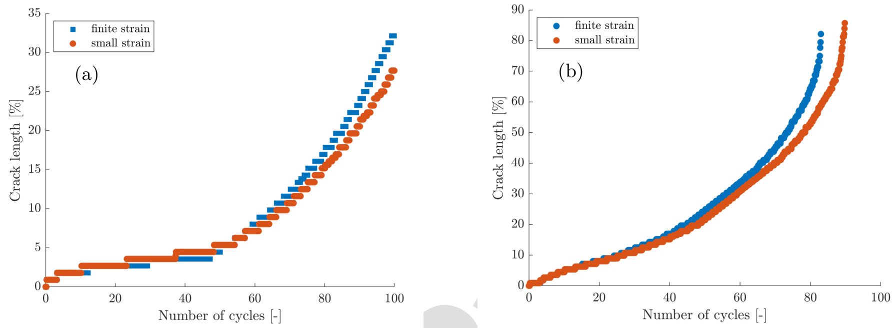

Figure A.21: Comparison between finite strain and small strain frameworks for (a) the initial configuration ($L_{comp}/t_{PCB} = 0.8$, $t_{comp}/t_{PCB} = 0.2$ and $t_{solder}/t_{PCB} = 0.015$) and for (b) a thin joint ($L_{comp}/t_{PCB} = 0.8$, $t_{comp}/t_{PCB} = 0.2$ and $t_{solder}/t_{PCB} = 0.004$).

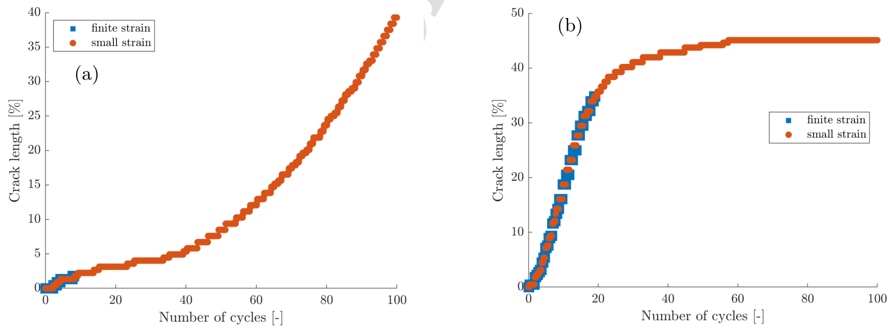

Figure A.22: Crack lengths calculated with a small strain setting for (a) a thick and small component ($L_{comp}/t_{PCB} = 0.5$, $t_{comp}/t_{PCB} = 0.3$ and $t_{solder}/t_{PCB} = 0.015$) and for (b) a thick solder joint ($L_{comp}/t_{PCB} = 0.8$, $t_{comp}/t_{PCB} = 0.2$ and $t_{solder}/t_{PCB} = 0.08$).

References

[1] R. N. Wild, Fatigue properties of solder joints, Welding research supplement (1972).

[2] R. Subrahmanyan, J. R. Wilcox, C.-Y. Li, A damage integral approach to thermal fatigue of solder joints, IEEE Transactions on Components, Hybrids, and Manufacturing Technology 12 (4) (1989) 480–491.

[3] J. Pang, D. Chong, T. Low, Thermal cycling analysis of flip-chip solder joint reliability, IEEE Transactions on Components and Packaging Technologies 24 (4) (2001) 705–712. doi:10.1109/6144.974964.

[4] L. Zhang, L. Sun, Y.-h. Guo, C.-w. He, Reliability of lead-free solder joints in csp device under thermal cycling, Journal of Materials Science: Materials in Electronics 25 (3) (2014) 1209–1213.

[5] Z. Cheng, G. Wang, L. Chen, J. Wilde, K. Becker, Viscoplastic anand model for solder alloys and its application, Soldering & Surface Mount Technology (2000).

[6] R. Darveaux, Effect of simulation methodology on solder joint crack growth correlation and fatigue life prediction, J. Electron. Packag. 124 (3) (2002) 147–154.

[7] J. H. Lau, Solder joint reliability: theory and applications, Springer Science & Business Media, 1991.

[8] J. Lau, Solder joint reliability of flip chip and plastic ball grid array assemblies under thermal, mechanical, and vibrational conditions, IEEE Transactions on Components, Packaging, and Manufacturing Technology: Part B 19 (4) (1996) 728–735. doi:10.1109/96.544363.

[9] A. Chaillot, M. Grieu, C. Munier, I. Lombaert-Valot, S. Bousquet, C. Chastanet, J. Canaud, R. Dumonteil, S. Villard, P. Raynal, et al., Fatigue life prediction models developed for green electronics in aeronautical and military communication systems (geamcos), in: EuroSimE 2009-10th International Conference on Thermal, Mechanical and Multi-Physics Simulation and Experiments in Microelectronics and Microsystems, IEEE, 2009, pp. 1–8.

[10] K. C. Norris, A. H. Landzberg, Reliability of controlled collapse interconnections, IBM Journal of Research and Development 13 (3) (1969) 266–271. doi:10.1147/rd.133.0266.

[11] W. Engelmaier, Functional cycles and surface mounting attachment reliability, Circuit World (1985).

[12] S. Ridout, C. Bailey, Review of methods to predict solder joint reliability under thermo-mechanical cycling, Fatigue & Fracture of Engineering Materials & Structures 30 (5) (2007) 400–412.

[13] H. D. Solomon, Strain-Life Behavior in 60/40 Solder, Journal of Electronic Packaging 111 (2) (1989) 75–82. doi:10.1115/1.3226525. URL https://doi.org/10.1115/1.3226525

[14] M. Erinc, P. Schreurs, M. Geers, Integrated numerical–experimental analysis of interfacial fatigue fracture in snagcu solder joints, International Journal of Solids and Structures 44 (17) (2007) 5680–5694.

[15] C. Basaran, C.-Y. Yan, A Thermodynamic Framework for Damage Mechanics of Solder Joints, Journal of Electronic Packaging 120 (4) (1998) 379–384. doi:10.1115/1.2792650. URL https://doi.org/10.1115/1.2792650

[16] H. Tang, C. Basaran, A damage mechanics-based fatigue life prediction model for solder joints, J. Electron. Packag. 125 (1) (2003) 120–125.

[17] ECSS, High reliability assembly for surface mount and through hole connections (2022).

[18] Keras API description, https://keras.io/api/, accessed: 2022-03-04.

[19] Keras API layer activation functions, https://keras.io/api/layers/activations/, accessed: 2022-03-04.

[20] Abaqus documentation, https://abaqus-docs.mit.edu/2017/English/SIMACAEEXCRefMap/simaexc-c-docproc.htm, accessed: 2022-04-26.

[21] Arlon 35n polyimide laminate and prepreg, https://www.arlonemd.com/wp-content/uploads/2020/04/35N.pdf, accessed: 2022-04-26.

[22] W. D. Jenkins, T. G. Digges, C. R. Johnson, Tensile properties of copper, nickel, and 70-percent-copper-30-percent-nickel and 30-percent-copper-70-percentnickel alloys at high temperatures, Journal of Research of the National Bureau of Standards 58 (1957) 201–211.

[23] G. Weber, L. Anand, Finite deformation constitutive equations and a time integration procedure for isotropic, hyperelastic-viscoplastic solids, Computer Methods in Applied Mechanics and Engineering 79 (2) (1990) 173–202. doi:https://doi.org/10.1016/0045-7825(90)90131-5.

[24] Y. Lee, C. Basaran, A Creep Model for Solder Alloys, Journal of Electronic Packaging 133 (4), 044501 (11 2011). doi:10.1115/1.4005288.

[25] A. Yeo, C. Lee, J. Pang, Flip chip solder joint reliability analysis using viscoplastic and elastic-plastic-creep constitutive models, IEEE Transactions on Components and Packaging Technologies 29 (2) (2006) 355–363. doi:10.1109/TCAPT.2006.875893.

[26] J. H. Pang, C. Seetoh, Z. Wang, Cbga solder joint reliability evaluation based on elastic-plastic-creep analysis, J. Electron. Packag. 122 (3) (2000) 255–261.

[27] C. Basaran, J. Jiang, Measuring intrinsic elastic modulus of pb/sn solder alloys, Mechanics of Materials 34 (6) (2002) 349–362. doi:https://doi.org/10.1016/S0167-6636(02)00131-X.

[28] W. Logsdon, P. Liaw, M. Burke, Fracture behavior of 63sn-37pb solder, Engineering Fracture Mechanics 36 (2) (1990) 183–218.

[29] Y.-H. Pao, A fracture mechanics approach to thermal fatigue life prediction of solder joints, IEEE transactions on components, hybrids, and manufacturing technology 15 (4) (1992) 559–570.

[30] S. E. Yamada SE, A fracture mechanics approach to soldered joint cracking, IEEE transactions on components, hybrids, and manufacturing technology 12 (1) (1989) 99–104.

[31] J. Hutchinson, A. Evans, Mechanics of materials: top-down approaches to fracture, Acta materialia 48 (1) (2000) 125–135.

[32] R. Tran, Z. Xu, B. Radhakrishnan, D. Winston, W. Sun, K. A. Persson, S. P. Ong, Surface energies of elemental crystals, Scientific data 3 (1) (2016) 1–13.

[33] T. L. Anderson, Fracture mechanics: fundamentals and applications, CRC press, 2017.

[34] P. Martiny, F. Lani, A. Kinloch, T. Pardoen, A multiscale parametric study of mode i fracture in metal-to-metal low-toughness adhesive joints, International journal of Fracture 173 (2) (2012) 105–133.

[35] T. Pardoen, T. Ferracin, C. Landis, F. Delannay, Constraint effects in adhesive joint fracture, Journal of the Mechanics and Physics of Solids 53 (9) (2005) 1951–1983. doi:https://doi.org/10.1016/j.jmps.2005.04.009.

[36] F. Van Loock, M. Thouless, N. Fleck, Tensile fracture of an adhesive joint: the role of crack length and of material mismatch, Journal of the Mechanics and Physics of Solids 130 (2019) 330–348. doi:https://doi.org/10.1016/j.jmps.2019.06.004.

[37] S. Dépinoy, F. Strepenne, T. Massart, S. Godet, T. Pardoen, Interface toughening in multilayered systems through compliant dissipative interlayers, Journal of the Mechanics and Physics of Solids 130 (2019) 1–20. doi:https://doi.org/10.1016/j.jmps.2019.05.013.

[38] J. V. van Zanten, G. Schuerink, A. Tullemans, R. Legtenberg, W. W. Wits, Method to determine thermoelastic material properties of constituent and copper-patterned layers of multilayer printed circuit boards, Journal of Materials Science: Materials in Electronics 29 (6) (2018) 4900–4914.

[39] B. Zhang, P.-k. Liu, H. Ding, W. Cao, Modeling of board-level package by finite element analysis and laser interferometer measurements, Microelectronics Reliability 50 (7) (2010) 1021–1027.

[40] H. Bunge, R. Ebert, F. Günther, On the angular variation and texture dependence of young's modulus in cold-rolled copper sheet, physica status solidi (b) 31 (2) (1969) 565–569.

- Fatigue tests are conducted on solder joints subjected to cyclic thermal loading.
- Machine learning methods reveal the effect of assembly parameters on joint failure.
- Finite element predictions are in agreement with identified experimental trends.
- Joint reliability increases with component termination length and solder thickness.
- Shear stresses at crack tip drive joint failure.

Declaration of interests

☒ The authors declare that they have no known competing financial interests or personal relationships that could have appeared to influence the work reported in this paper.

☐ The authors declare the following financial interests/personal relationships which may be considered as potential competing interests: